Materials Physics and Mechanics 32 (2017) 222-236 Received: September 2, 2016

IN-SITU MEASUREMENT AND FINITE ELEMENT SIMULATION OF THERMO-MECHANICAL PROPERTIES OF AA 6063 ALUMINUM ALLOY FOR MIG WELDMENT

S. Baharnezhad [1*], A. P. Golhin [2]

[1]Department of mechanical engineering, École Polytechnique de Montréal, Canada

[2]Department of mechanical engineering, KN Toosi University of Technology, Iran

[*]e-mail: sadreddin.baharnezhad@polymtl.ca

Abstract. The *metal inert gas* (MIG) welding and the crucial parameters influenced on the thermal and mechanical behaviours, and microstructure of AA 6063 aluminum were investigated through the experiment and the FE simulation. A thermo-mechanical model was extended using the finite element software of ABAQUS. In this manner, the thermal distribution and time-temperature histories made during MIG welding were derived. To achieve more accuracy, a subroutine was developed by FORTRAN. The real-time temperature measurements and the effective parameters of the thermal distribution, including the welding speed and the arc voltage were studied by conducting MIG bead-on-plate welds and the residual stresses derived from the simulation were compared with the empirical observations. The results depicted that the simulation would estimate rigorously the temperature gradients and the fields of welding-induced stress. The microstructural and microhardness examinations were also conducted which allowed—alongside the TTT curve—the phases precipitated and the heat sink effects were studied and foreseen. Indeed, the microstructure images demonstrated that the overaged, agglomerated β-Mg_2Si phases, in the HAZ, and the modified β-AlFeSi pseudo-plate-like precipitates alongside the smaller and coarsened β-Mg_2Si phases, in the fusion zone, were precipitated.

Keywords: FE simulation, in-situ measurement, 6063 aluminum, welding residual stress, thermo-mechanical properties, TTT curve, microstructural examination.

1. Introduction

Welding of aluminium alloys has been always faced several challenges. Despite the high weldability properties of this metal, such limitations as high thermal conductivity, remarkable thermal expansion and contraction, low melting point, and many changes in the structure and properties shall be considered in in the welding processes [1,2]. Hence, in the aluminium joints, examination of welding processes, and consequently, the distribution of stress and heat on mechanical properties are of great importance. Distribution of residual thermal stress of welding depends upon several factors such as pieces size, specifications of materials, constraint conditions, heat input, type of joining, number of welding passes and their sequence, mixture of gases and metal transferring mode. Examination of all these factors during welding of different aluminum alloys is highly complicated and costly [3-7]. One of the interesting aluminum alloys for researchers and industry is AA6063 due to having a good weldability and its widespread applications in some of important industries such as defense, aerospace and automobile.

Simulation is widely used in the development of the research, production, and industrial processes today. Finite element method (FEM) is one of the most applied numerical techniques, which is employed in the various engineering sciences [8-11]. Accordingly, many models have been presented for simulation of the effect of various welding parameters on the base metal properties that can be analyzed by different numerical methods [12-14]. The results revealed that for a thin sheet, the temperature history of whole volumetric loading would comply with the empirical measurements. Goldak and his research team suggested a double ellipsoidal model, as a heat source, to raise accuracy of the results. They also introduced this model as a deep penetration welding model [15]. The main idea of this method is a Gaussian distribution of heat input on a double ellipsoidal as shown in Fig. 1. Guo *et al.* [16] studied on the formation of cold weld in Gas Metal Arc Welding (GMAW) of aluminum alloy 6005-T4 using experimental and numerical methods. They proposed three methods of heat inputting to enhance the weld penetration at the initial welding state. They also obtained the final weld profile and the maximum temperature in the HAZ. Their research was supported by some metallurgical characterizations and microhardness examinations. Anca et al. simulated an arc welding thermo-mechanically by FEM. They predicted the thermal histories and the residual stresses [14].

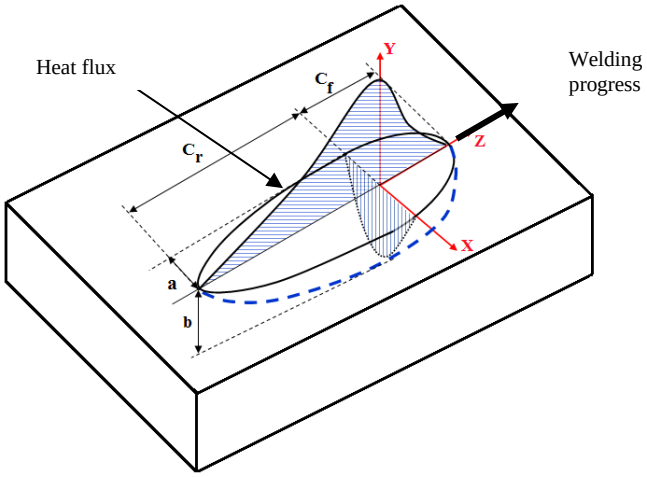

Fig. 1. Schematic of the double ellipsoid heat source configuration.

Chen et al. [17] investigated the thermal and mechanical behaviour of the weldments during arc welding using the experimental and numerical method. They developed a new technique for high temperature strain measurement in their experimental efforts so that they could measure the strain in a distance of 1 mm away from the fusion line. Meanwhile, they used the FEM to approve their claim.

Considering the effect of Metal Inert Gas (MIG) welding parameters on the mechanical properties of aluminum alloy 6063 joints, the finite element method was used as a high-precision approach in the present research. Also, in order to model the two-weld passes and import the molten elements into fusion zone, element birth and death technique was used. Simulation and analysis process was made by ABAQUS software in standard mode. To achieve a more accurate solution and use the moving heat source, a subroutine was developed in FORTRAN. The simulation output was compared with the experimental results. The results showed that the simulation would to forecast the thermal transient profile, the range of heat affected zone and the extension of residual stresses.

Based on the authors' knowledge, this is the first in the literature that reports the analysis of 6063 Al via both experimental GMAW and FEM by considering the time-dependent thermal and mechanical properties, real-time temperature measurements, including fusion zone, and

microstructure examinations. Previous studies focused mainly on the other Al grades and were more experimental, however, few studies on welding of Al 6063 for both empirical and numerical have been reported.

Nomenclature:

c	Thermal capacity, J. kg^{-1}. K^{-1}
C_{ijkl}	Elastic tensor
$d\varepsilon_{ij^e}$	Elastic strain
$d\varepsilon_{ij^p}$	Plastic strain
$d\varepsilon_{ij^{th}}$	Thermal strain
q	Thermal current density, J. m^{-1}. K^{-1}
q_s	Constant thermal flux at the surface, J. m-1. K-1
T_s	Surface temperature
T_{sur}	Surrounding environment temperature ،K
T_∞	Temperature of the fluid in contact with the work piece, K
σ_{sb}	Stefan-Boltzmann constant, 5.6704e-8 J. m^{-2}. s^{-1}.K^{-4}
ε	Whole-body heat transfer coefficient
η	Surface normal axis
λ	Thermal conductivity coefficient, J. m^{-1}. s^{-1}.K^{-1}
ρ	Density, kg^{-1}. m^{-3}
$\dot{Q}$	Energy generation rate, W. m^{-3}

2. Simulation

Finite element software of ABAQUS 6.10-1 was employed for modelling, mechanical and thermal analyses in this research. The schematic of the cross-section profile, with the welding sequence, and the 3-D finite element model of the thermal coupling of the joints is illustrated in Figs. 2 and 3, respectively.

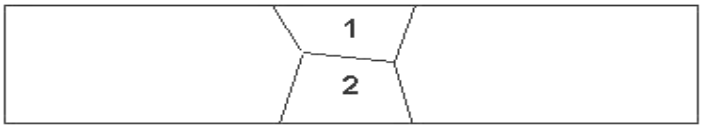

Fig. 2. Schematic of two-pass weld sequence used in the simulation.

Considering the symmetry, half of the shape geometry, has been modelled. Due to the high temperature gradient and stress in the heat-affected zone (HAZ), and to enhance the analysis precision, a higher element density was opted for these regions. In contrast, in order to increase the analytical convergence rate, and consequently, to reduce the solving time, the larger mesh sizes were provided for the farther regions. Also, the uncoupled thermo-mechanical analysis and the element birth-and-death technique were used to model the weld passes and filler metal deposition. In fact, three fields of heat, metallurgy, and mechanics are in contrast in the modelling of the welding process. The relationship of these three fields is cleared by choosing an analysis method for welding simulation. Since thermal and mechanical properties are correlated in FE modelling of weld and affect the metallurgical quality of weldment, hence both thermal and mechanical differential equations must be solved as correlated. Because of the low heat generated by the plastic strain while welding, the effect of surface strains on surface heat transfer coefficient can be ignored. Hence, the thermal and mechanical equations can be independently solved [15, 18-20]. Therefore, the present research used an uncoupled solution and the residual stress field was generated by elastic-plastic analysis.

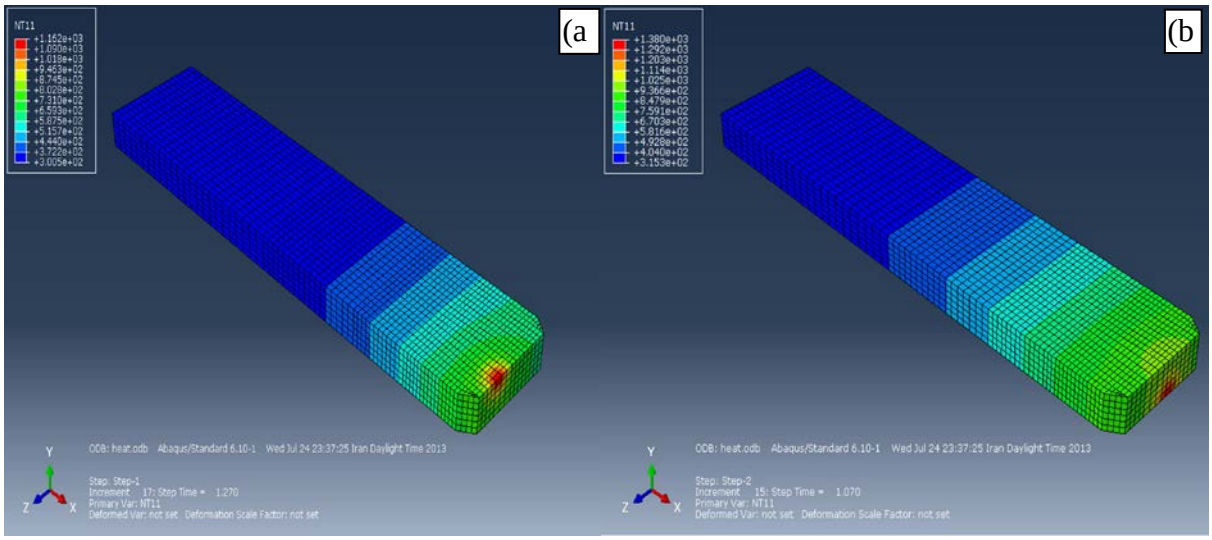

Fig. 3. Three-dimensional finite element model of the thermal coupling, (a) pass 1, (b) pass 2.

2.1. Thermal analysis. Heat transfer in welding is time-dependent and temperature distribution in an object is non-uniform and is a function of the spatial and temporal coordinates. Then, the time-dependent heat transfer equations are used to analyse this process. The principle of conservation of energy and Fourier's law can be used to explain the differential equation of heat transfer independently from the strain generated as per Eq. 1:

$$pc\frac{\partial T}{\partial t} = \nabla.\left(\lambda \nabla T\right) + Q \tag{1}$$

In this relation, c is the heat capacity, ρ is the density, λ is the thermal conductivity coefficient, and Ơ is the energy generation rate. Since the heat equation derivatives degrees are first order and quadratic regarding spatial and temporal coordinates, respectively, two boundary conditions and one initial condition are required for describing the system. The common boundary conditions often used in the thermal issues of welding are Dirichlet and Neumann boundary conditions proposed in the Eqs. 2 and 3, respectively [18]:

$$T = T_s, \tag{2}$$

where this is the surface temperature which is constant.

$$\{q\}^T\{\eta\} = -q_s \tag{3}$$

The Neumann condition refers to a given heat flux where η is the surface normal vector, q is the heat-flow density, and q_s is the constant heat flux at the surface. Insulated or adiabatic surface and the surface displacement are also according to Eqs. 4 and 5:

$$\{q\}^T\{\eta\} = 0 \tag{4}$$

$$\{q\}^T\{\eta\} = h_c(T_s - T_\infty), \tag{5}$$

where T_∞ is the fluid temperature in contact with the piece, T_s is the surface temperature, and h_c is the heat transfer coefficient of the object displacement (a function of temperature, surface position, and fluid velocity).

Radiation on the surface is calculated by Stefan Boltzmann law in Eq. 6:

$$\{q\}^T\{\eta\} = \varepsilon\sigma_{sb}(T_s^4 - T_{sur}^4), \tag{6}$$

where T_{sur} is the ambient temperature, Ɛ is the object export coefficient, and σ_{sb} is constant of Stefan Boltzmann.

Heat flux was applied in mobile welding as a mobile thermal-volume source with an elliptical distribution of type of Goldak model [21]. To this end, a subroutine was written in FORTRAN language for applying heat flux in a 3-D model. In addition, for being close to the real conditions, all the mechanical and thermal properties were considered, based upon the data sources of Al6063 alloy spread by the references such as JMatPro software and ALLUSELECT,

temperature-dependent [22-24]. The heat flux equation in the front and back of the heat source was obtained by Eqs. 7 and 8.

$$q_f(x,y,z,t) = \frac{6\sqrt{3}f_f Q}{abc_f \pi\sqrt{\pi}} e^{-3x^2/a^2} e^{-3y^2/b^2} e^{-3z^2/c_f{}^2} \quad (7)$$

$$q_r(x,y,z,t) = \frac{6\sqrt{3}f_r Q}{abc_r \pi\sqrt{\pi}} e^{-3x^2/a^2} e^{-3y^2/b^2} e^{-3z^2/c_r{}^2} \quad (8)$$

In the above equations, the spatial coordinates of x and y are functions of time. Also, f_r= 1.4, f_f=0.6 so that f_r+f_f=2 [15], and parameters of C_f, C_r, b, and a are experimentally measured by cross-section properties of the weld pool and of the heat affected zone.

2.2. Stress analysis. For mechanical analysis of the temperature record, the thermal analysis was used as an input. Thermal stress and strain were also calculated in each temporal phase and the final state of the residual stress was obtained by the accumulation of thermal stresses and strains in the end-stage cooling. In welding process in which elastic-plastic deformation is made, the balance equations for the stress-strain rate are obtained by the following equation [25]:

$$d\sigma_{ij} = C_{ijkl} d\varepsilon_{kl}{}^{e} = C_{ijkl}\left(d\varepsilon_{kl} - d\varepsilon_{kl}{}^{p} - d\varepsilon_{kl}{}^{th}\right), \quad (9)$$

where C_{ijkl} is the elasticity tensor which includes Young's modulus and Poisson's ratio, $d\varepsilon_{ij}{}^{e}$ is elastic strain, $d\varepsilon_{ij}{}^{p}$ is plastic strain, and $d\varepsilon_{ij}{}^{th}$ is thermal strain.

Flow rules such as Prandtl-Reuss relations are used in the plastic zone. Given the associative flow rule, plastic flow direction is perpendicular to the surrender. In this rule, it is assumed that small plastic strain $d\varepsilon_{ij}{}^{p}$ is proportional to perverted tensions in every moment of loading. Therefore, the small plastic strain is obtained as Eq. 10,

$$d\varepsilon_{ij}^{p} = \frac{3}{2}\frac{d\varepsilon_p^{eq}}{\sigma^{eq}} S_{ij}, \quad (10)$$

in which:

$$d\varepsilon_p^{eq} = \sqrt{\frac{2}{3} d\varepsilon_{ij}^{p}\, d\varepsilon_{ij}^{p}} \quad (11)$$

$$\sigma^{eq} = \sqrt{\frac{3}{2} S_{ij} S_{ij}}, \quad (12)$$

where $\delta^{eq} = \delta_{yp}$ indicates the onset of plastic change in a moment and δ_{yp} value changes with temperature.

Yield stress of metals also increases by growing plastic strain [15,18-20]. Owing to imposing alternate tensile and compressive stresses to the object during welding, it should use the kinematic work hardening model [15,18,19]. Thus, a kinematic work hardening curve was considered based on the plastic strain at different temperatures. In the mechanical analysis, a linear eight-node cube element was employed, and the thermal history of the thermal analysis is imposed to the model as a thermal load. Then, the resulting stresses and strains are calculated by an elastic-plastic analysis of the object in every time interval. This operation is continued until the intended model gets cold at the ambient temperature. The calculated values in the final phase indicate welding residual stresses and strains [15,18-20].

3. Experimental procedures

3.1. Preparation of the coupons and temperature measurement. To prepare the coupons, among the sheets provided by the bus manufacturer, Oghab Afshan Co, some aluminum sheets of 6063 alloys in the size of 45×11×3 mm^3 were cut.

Upon surface preparing, the coupons underwent MIG welding by considering the input parameters such as flow rate, voltage, wire feeding speed, welding speed, etc. The final schematic of the coupons made for stress test is the same as depicted in Fig. 4.

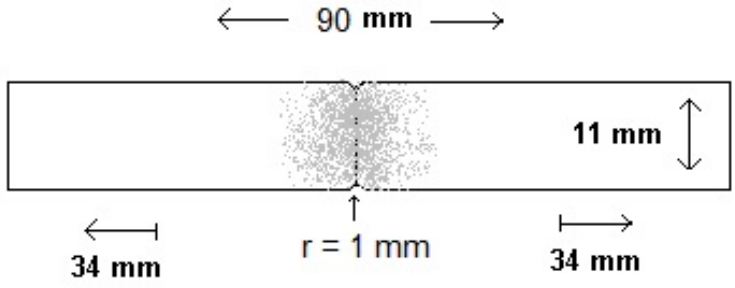

Fig. 4. Schematic of the tensile specimen welded by MIG.

To make the required welding connections, MIG machine MegaMax-SP500 with a rectifier was used. Welding gas source contained 100% argon with the shielding gas blowing rate of 15 Lit/min and recommended filler wire of ER5356 with a diameter of ½ mm and wire feeding speed of 10 m/min [26]. Table 1 shows the results of the chemical analysis of the parent metal and the filler wire used. The current source for all coupons was three-phase DC with output current of 110 ampere. Some suitable fixtures were used to stabilize the coupons and prevent from distortion during welding. The coupons were also cleaned up before welding by diluting phosphoric acid 5% and alcohol.

Table 1. Chemical compositions of the parent material and filler wire used [wt%].

Composition	Mg	Si	Fe	Mn	Zn	Cu	Cr	Ti	Al
Al 6063	0.75	0.45	0.26	0.08	0.07	0.03	0.02	0.01	Bal.
ER5356	5.1	0.27	0.43	0.11	0.10	0.10	0.90	0.80	Bal.

The manually welding was performed by a qualified welder in the butt joint. To determine the welding speed, trial and error were performed by a chronometer to make a suitable weld. The examined welding parameters were as per table 2.

Table 2. Welding operation parameters.

Coupons No.	Voltage [V]	Welding speed [mm/s]
1	5	1.66
2	5	2.50
3	5	5.00
4	3	2.50
5	6	2.50
6	9	2.50

The temperature at the different position the coupon was measured using the calibrated infrared thermometer (RayTek-RAY3IPLUS2M) with a spectral response of 1.6 microns, and with ±1% accuracy [27]. The IR thermometer was stabilized on the back side of the specimen and adjusted to record the temperatures-times at the 3 positions, parent metal, HAZ, and fusion line with the distance of 2, 6 and 15 mm from the weld centerline, respectively. These positions have been depicted in Fig 5-a.

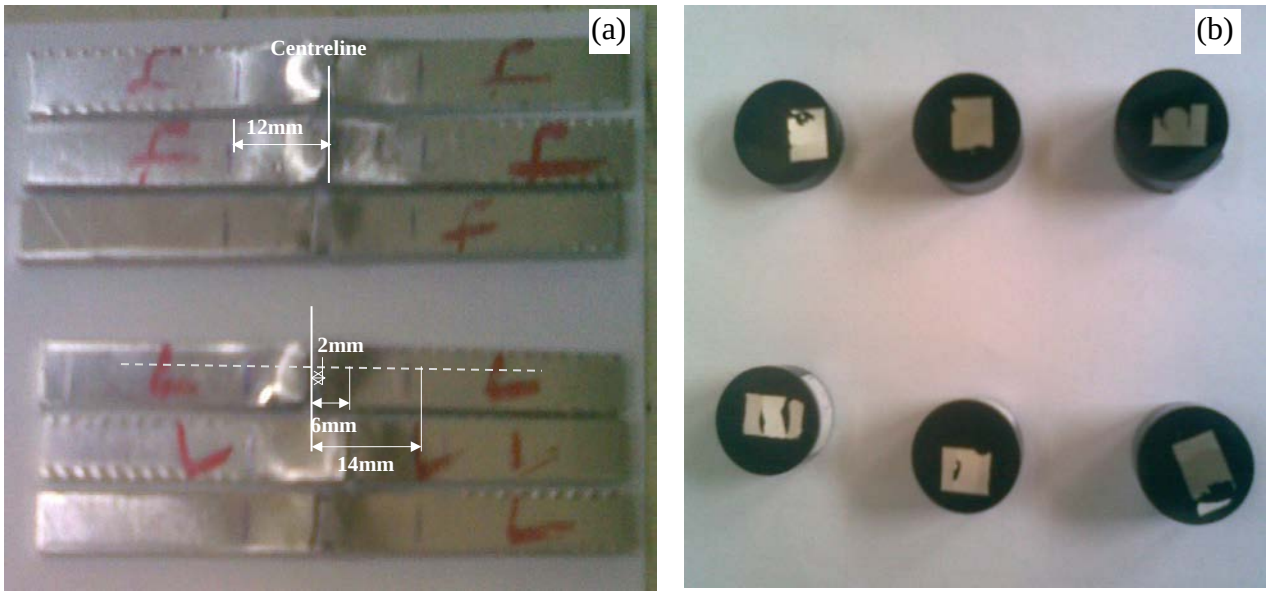

Fig. 5. The coupons of the 6063 Al sheets welded using MIG (a) distorted zones in the tensile test coupons, and (b) cross-section of the weld profile and the hardness test coupons.

3.2. Tensile test. To examine the tensile behaviour of the welded joints, the universal testing machine (Dartec model) was used. Flat jaw has been used in this research and the lower jaw was fixed and the upper one was mobile during the test. The tensile force ranges from 0 to 100 KN was imposed to the test coupons by the fixed velocity of 0.025 KN/s. In fact, six test coupons were prepared to conduct the tensile tests with the three various welding speeds and three operating voltages. The result contains the graphs of the engineering stress versus the engineering strain value.

3.3. Microhardness testing. A microhardness testing machine (InnovaTest 422A) was employed to measure the hardness at the 3 desired regions, fusion line, HAZ and parent metal. The Vickers hardness was conducted under a test force of 200 gr. To raise accuracy of the results, each hardness test was repeated three times and their averages were reported versus the specified distance from the fusion line.

3.4. Microstructural examination. To prepare the coupons of metallography, the welded zone in each sheet was separated by cutting and was, then, polished. To etch the coupons, the mixture solution of HCL 15%, HNO3 25%, HF 1% was used within 2 minutes in environmental conditions. For image capturing and measuring, the optical microscope (Leica DM1750 M) was employed by the Clemex software.

4. Results and discussion

4.1. Simulation output and comparison with the experimental results. The output from simulation analysis of the residual stresses can be seen in Figs. 6 and 7. According to the obtained results, the distorted zone is in approximately 10 mm of the weld line (Fig. 6) that is in good agreement with the observations (12 mm in Fig. 5 (a)).

As seen in Fig. 6, the residual stresses of the model simulated are compressive in the interval of 4-11 mm, and are tensile before the interval. The related 3D picture of the FEM model can be seen in Fig. 7.

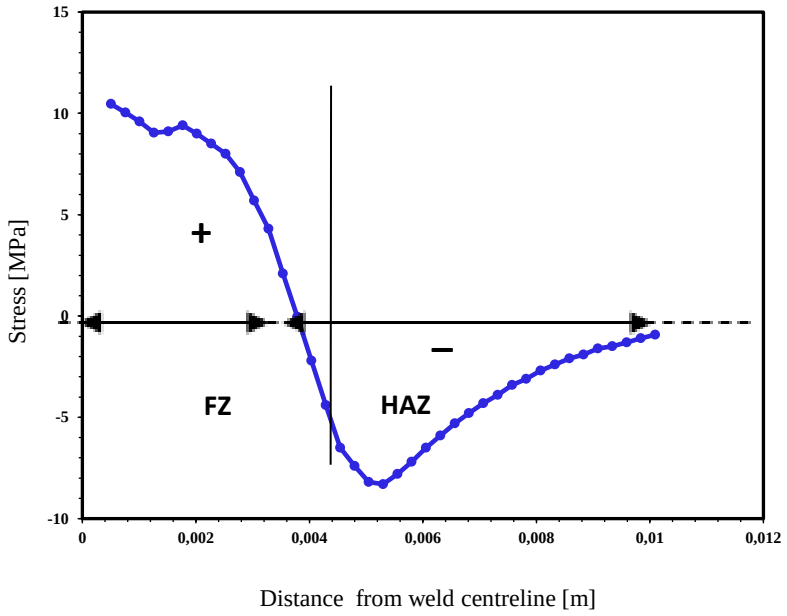

Fig. 6. The residual stress distribution in the HAZ and the fusion zone, at t=250s, perpendicular to the weld line, derived by the simulation.

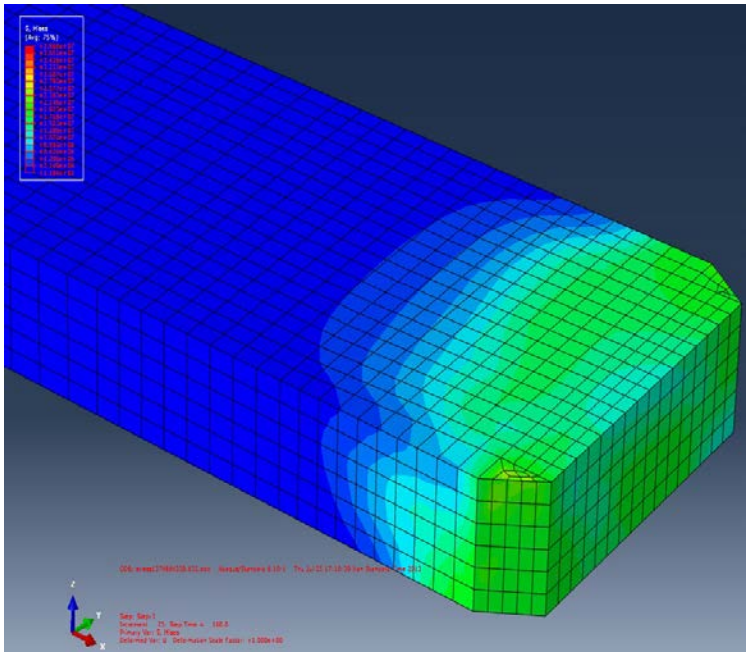

Fig. 7. Von Mises residual stress of the welded model.

4.2. Transient temperature analysis. Both the in-situ transient temperature measurements at 3 positions of the fusion line (FL) and HAZ, and the parent metal (PL) and those were calculated aiding the finite element method described above are compared in Fig. 8 (a) to (c), respectively. The diagrams demonstrate that the FEM values are in good conformity with the measured ones in terms of both trends and magnitude. The diagrams of a and b also depict how they follow a similar pattern so that they all reach a peak abruptly, and then, drop dramatically due to the strong heat sink, and eventually, decline steadily over the period. But Fig. 8 (c) depicted that how this rate has been much moderate, in contrast with the steel alloys which have an abrupt decrease, owing to the high rate of heat arrived from the previous transferred paths.

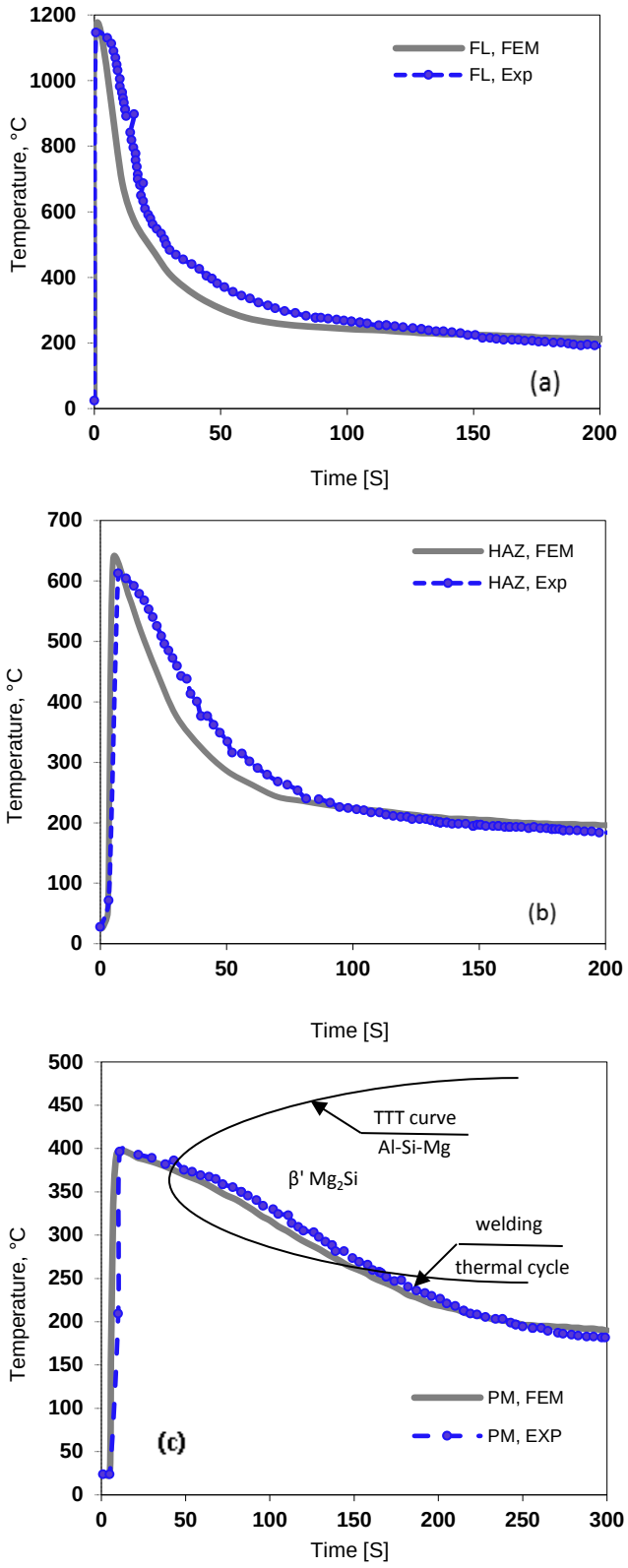

Fig. 8. Comparison between diagrams of the FEM and the in-situ temperature measurements for MIG welding of the 6063 Al sheets at the three regions, (a) the fusion line (FL), (b) the HAZ (FL+4), and (c) the parent metal (FL+12) alongside the TTT curve.

Since the temperature of the molten pool in GMAW of aluminum alloys is higher than 1227 °C, [28] compared to the melting range of the alloy that is between 616 to 654 °C, it is possible to increase the wire feeding speed that in return increases the deposition rate, which is

an economically considerable effect, especially when this also can be led to reach a soundness weld without increasing the risk of imperfections like as lack of fusion. Fig. 9 depicts a good agreement between the maximum temperatures forecasted and those were measured in the real-life experiment so that these values in the FZ were 1161°C and 1149°C, respectively. Fig. 8 (a) particularly depicted that because of the large heat sink phenomenon, the parent metals have not been fused at the very start-up of the welding so that there were been the thresholds in this regard.

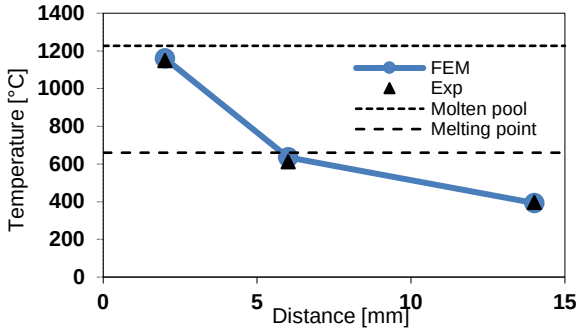

Fig. 9. Comparison between the experimental peak temperature measurements with the ones derived from the FEM vs. the distance from the fusion line. The average molten pool [28] and melting point temperatures were drawn as indicators.

4.3. Mechanical properties. As depicted in Fig. 10 (a), the more the welding speed, the more stress-strain values such that for the coupon (1), with the lowest welding speed, the conventional yield stress is 4.84 MPa, for the coupon (2), with the average speed, is 9.68 MPa, and for the coupon (3), with the highest welding speed, is 16.13 MPa. The ultimate tensile strength (UTS) for the coupons of (1), (2) and (3) were also 12.9, 26.45, and 45.16 MPa, respectively. Both of the above data were ascending and revealed that the UTSs were improved by increasing the welding speed and due to decrease the heat input.

The contrary is true for the arc voltage (Fig. 10 (b)). It means that by increasing the arc voltage, the tensile properties are decreased. Therefore, the conventional yield stress is 16.13 MPa with the low arc voltage in the coupon (4), 6.45 MPa with the average arc voltage in the coupon (5), and 6.05 MPa with the high arc voltage in the coupon (6). The ultimate strengths for the coupons 4, 5, 6 were also 41.29, 24.19, and 15.48 MPa, respectively, which has a descending trend.

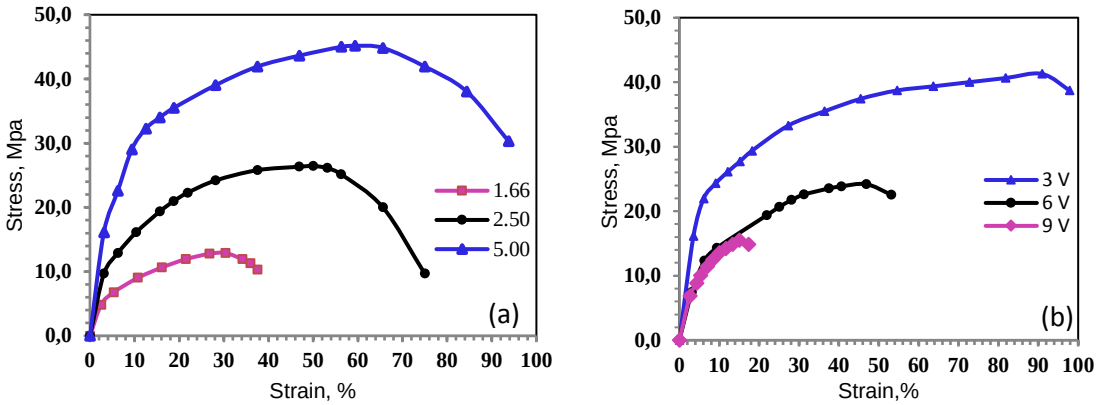

Fig. 10. The tensile test diagrams of the 6063 Al coupons welded by MIG in variant (a) welding speed [mm/s], and (b) voltage [v].

Fig. 11 (a) depicts that the hardness goes up by increasing the welding speed while the hardness curves move towards the smaller numbers by voltage increasing as depicted in Fig. 11 (b). The results are well-adapted to the data obtained from the simulation and the stress-strain curves. The dramatic drop in the sides of each curve is related to the HAZ which depicts much less hardness in comparison with the fusion zone (middle of the curves).

Considering the hardness values obtained and the average of 83 Vickers for the primary aluminum 6063 coupons, heat-affected zones have less hardness of approximately 20 units in Vickers scale. This observed feebleness in the HAZ was owing to the overaging, the partial dissolution, and the formation of undesired precipitations during the welding heat input cycle. To eliminate this deficiency and increase hardness of the weld surrounding zones, rolling down the weldment and explosive tapping are performed after thermal processing followed by welding. Recently, modern methods such as hardening by the pulsed laser beam and/or high-energy electron beams have been suggested. In both of the above tapping methods, hardness increases by work hardening mechanism. According to the information provided by the supplier, the primary parent metal of Al 6063 alloy contained 4.23% of fine phase of Mg_2Si.

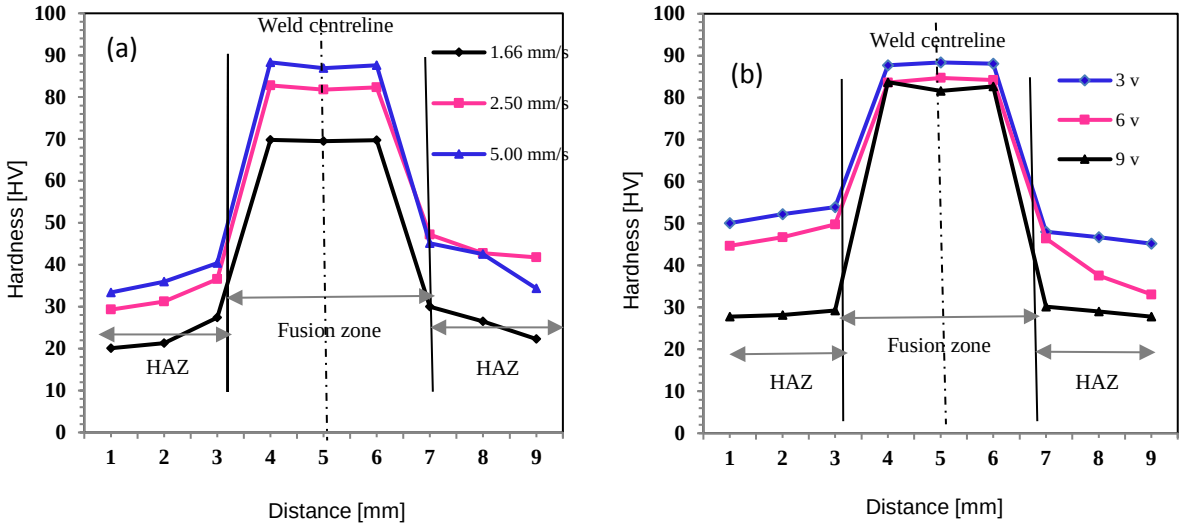

Fig. 11. The diagrams of hardness vs. mirror distance of the 6063 Al coupons welded by MIG with 2 specified regions: the fusion zone (FZ) and the HAZ, in the variant of (a) welding speed, and (b) voltage.

After welding, the computer analysis of the coupon images by Clemex software depicted that the mean percentage of the finer and darker phase of Mg_2Si is 2.27% (Fig. 12 (a)). This indicated a decrease in precipitation percentage after welding probably due to dissolution of precipitates exposed to welding heat. Reduction of precipitate percentage and grading structure shall be the result of the partial anneal in the HAZ accompanied by the dissolution and/or decomposition of the precipitates. If the diffusion circumstances are provided in the surrounding weld line, the hardness raises by increasing the precipitates percentage and their uniform dispersion in the matrix. Moreover, welding of 6063 Al alloy not only causes to eliminate the primary aging, but also brings to lose the dislocation density, their alignment and order which had been made from the previous cold work [1,29]. The dilution of the Mg_2Si percentage of the parent material is indeed crucial by using an appropriate filler metal to reduce the weld metal crack susceptibility.

As a modal comparison between the studied alloy and 6061 alloy, as the most analogous grade for that, since the 6063 alloy is more diluted than 6061 one (has the lower contents of Si

and Fe), the amount of $Al_xFe_ySi_z$ spreads (i.e $FeAl_3$, $FeAl_6$, Fe_3SiAl_{12}, Mg_2Si in a wrought form) [26] is not so sufficient, consequently, their mechanical properties are not greatly affected by its low cooling rate [30]. Besides, pursuant to the time-temperature transformation (TTT) curves reported in some literatures [31,32], whereas in the TTT curves of the alloy studied, the critical temperature range (the hardness falls down rapidly with the extension of isothermal time) is 300 to 410 °C and the nose temperature is 360 °C, however, compared with those values of 6061 Al which are 220 to 440 °C and 360 °C, respectively, it can be perceived that there is a lower percentage of the precipitates in 6063 alloy which that our observations demonstrated the same.

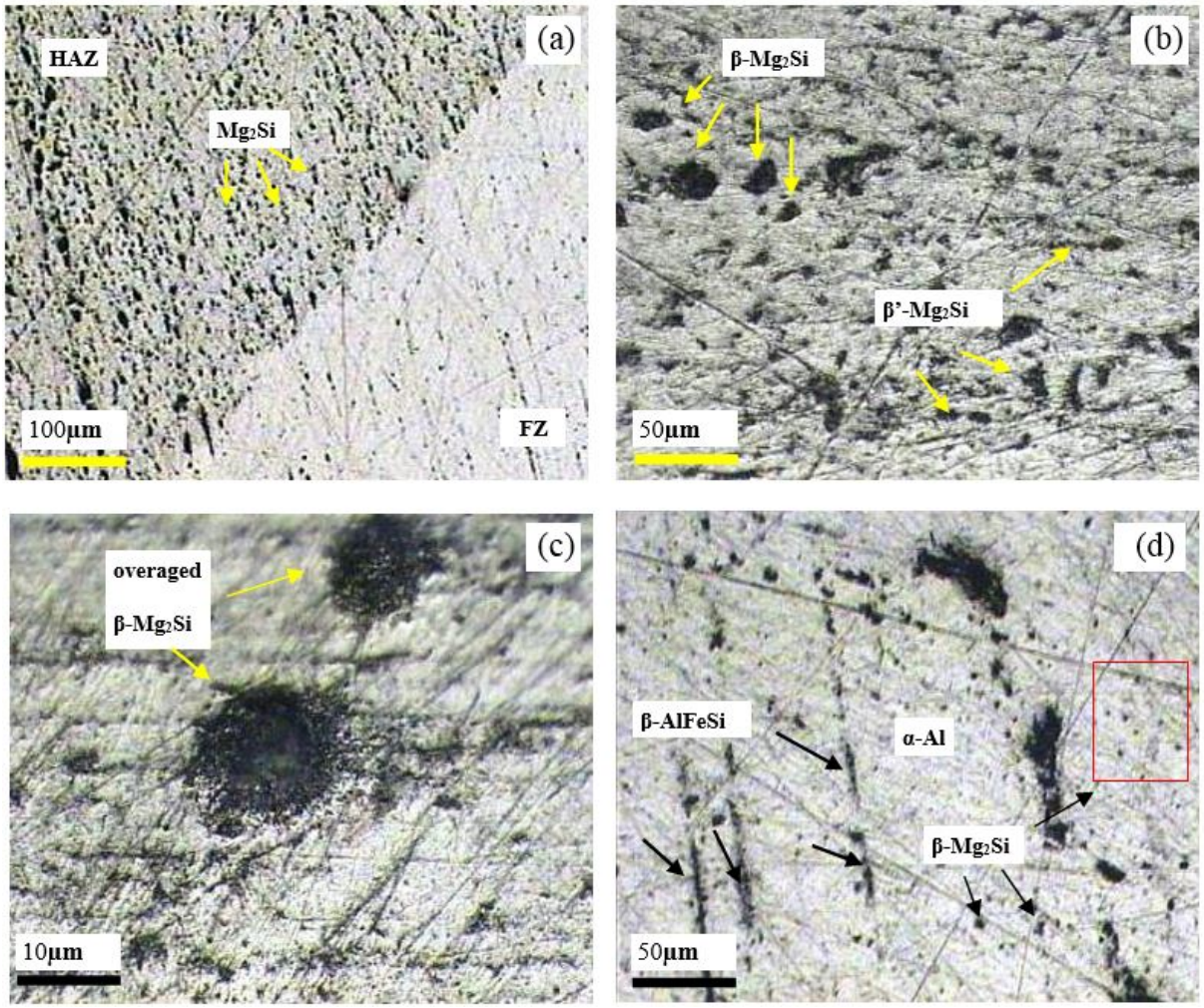

Fig.12. The microstrucure images of the welded 6063 Al alloy, (a) the boundary between HAZ and FZ with the phases precipitated, (b) HAZ, (c) the overaged, agglomerated β-Mg_2Si in HAZ, and (d) Modified β-AlFeSi pseudo-plate-like with the smaller and coarsened β-Mg2Si precipitates in the FZ.

As depicted in Fig 12. b and c, HAZ has a microstructure with the overaged and rounded black precipitates containing β-Mg_2Si precipitates, equilibrium phase with a FCC crystal structure, were dispersed in the matrix. This region also may contain a little amount of the coarsened β'-Mg_2Si precipitates, developed rod-like with a hexagonal crystal structure, as the TTT curve forecasted it. The FZ is distinguished by its pseudo-plate-like dendrites, which contains the dark inter-dendritic network called β-AlFeSi as shown in Fig.12 (d). In fact, these kind of precipitates are not exactly a plate-like, similar to what might see in the cast ingot, their shapes are partially modified from plate to sub-plate, owing to a rapid cooling rate of welding.

This region also contains, the finer Mg_2Si precipitates. These results are consistent with the findings of other researchers [16, 33-38].

Indeed, the TTT curve in Fig. 8 (c) depicts that the probability of formation of β'-Mg_2Si precipitates is not high, but by and large its trend is to increase by moving from FZ towards HAZ.

5. Conclusions

In this research, the welding simulation package of MIG welding of Al 6063 alloy was developed and the influences of the microstructure, thermal history and heat input, and some other crucial welding parameters, including velocity and voltage, on the mechanical and physical features of the welded alloy were examined. The main results of the empirical examinations and the simulation are as follows:

– The results of tensile and micro-hardness measurements indicated that the increase in the welding speed results in increasing hardness, tensile strength, and yield stress in 6063 aluminum alloy. While increasing in arc voltage results in decreasing in the above values.

– The results of the temperature gradients and the fields of welding-induced stress depicted that there is a good agreement between the simulation and the real-life measurements for the alloy. Actually, based on the FEM results, the distorted zones were extended along the weld centreline up to 10 mm. This almost had a compliment with the empirical observation, which was 12 mm. Indeed, the compressive thermal stresses were developed in the vicinity of the fusion line. Furthermore, the simulation results depicted that the residual stress on the intended model are compressive in the interval of 4 to 11 mm, from the weld centreline, and is tensile out of that which are in good accord with the experimental findings in terms of the appearance of the weldment.

– Based on both results of the FEM and the real-life temperature measurements, it has been found that owing to the large heat sink phenomenon, the parent metals have not been fused at the very start-up of the welding so that there were been the thresholds in this regard.

– The microstructural and microhardness examinations also illustrated that the parent metals have been heated up—partially annealed—moderately during the welding. The microstructure images depicted that the overaged, agglomerated β-Mg_2Si phases, in the HAZ, and the β-AlFeSi pseudo-plate-like precipitates alongside the smaller and coarsened β-Mg_2Si, in the fusion zone, were precipitated. Moreover, a lower amount of β-Mg_2Si participates for the 6063 Al sheets in comparison to the 6061 one were found which was in accord with the predictions (considering the TTT curve) and those reported in the some literatures.

– The in-situ temperature measurements in the fusion zone and the HAZ made ability to foresee and analyze the phases participated and the related mechanical behaviour in the weldment. For instance, the TTT curves depicted that how by moving from the fusion line towards the HAZ, and beyond, the various cooling rates may lead up to the precipitation of β'-Mg_2Si.

Acknowledgment. *The authors express their gratitude to Prof. A. H. Raeouf for his advice, the department of metallurgy and materials, faculty of engineering of Semanan University and the automobile company, Oghab Afshan Co., for the lab facilities and materials supports.*

References

[1] M. Mathers, *The welding of aluminum and its alloys* (Woodhead Publishing Ltd., Cambridge, England, 2002).

[2] M. Olabode, P. Kah, J. Martikainen // *Proceedings of the Institution of Mechanical Engineers Part B Journal of Engineering Manufacture* **227** (2013) 1129.

[3] M.A. Wahab, MJ Painter, M.H. Davies // *Journal of Materials Processing Technology* **77** (1998) 233.
[4] C. S. Chen, J. G. Yang, A. H. Tan // *Materials Science and Technology* **25** (2009) 896.
[5] J. Chen, C. Schwenk, C.S. Wu, M. Rethmeier // *International Journal of Heat and Mass Transfer* **55** (2012) 102.
[6] Y. Tsujimura, S. Nakanishi, A.B. Murphy, M. Tanaka // Q*uarterly journal of the japan welding society* **21** (2013) 5s-8s.
[7] R. P. Verma, K.N. Pandey,Y. Sharma // *Proceedings of the Institution of Mechanical Engineers Part B Journal of Engineering Manufacture* **229** (2015) 1021.
[8] J. A. Goldak, M. Akhlaghi, *Computational welding mechanics* (Springer, New York, USA, 2005).
[9] W. Bleck, U. Reisgen, O. Mokrov, E. Rossiter, T. Rieger // *Advanced Engineering Materials* **12** (2010) 147.
[10] J. Hu, H. L. Tsai // *Journal of Physics D: Applied Physics* **41** (2008) 065202.
[11] S. Baharnezhad, H. Farhangi, A. A. Allahyari // *Journal of Mechanics in Medicine and B iology* **13** (2013) 1.
[12] P.H. Chang, T.L. Teng // *Computational Materials Science* **29** (2003) 511.
[13] C.K. Takemori, T.D. Müller, M.A. De Oliveira, *Numerical simulation of transient heat transfer during welding process*, In: *Int. Compress Eng. Conf.* (Purdue, USA 2010).
[14] A. Anca, A. Cardona, J. Risso, V.D Fachinotti // *Applied Mathematical Modelling* **35** (2011) 688.
[15] J.A. Goldak, A.A. Chakravarti // *Metal. Trans.***15** (1984) 200.
[16] H. Guo, J. Hu, H.L. Tsai // *Numerical Heat Transfer, Part A: Applications* **57** (2010) 392.
[17] J. Chen J, X. Yu, R.G. Miller, Z. Feng // *Science and Technology of Welding & Joining* **20** (2015)181.
[18] A. Kermanpur, M. Shamanian, V. Esfahani Yeganeh // *Journal of Materials Processing Technology* **199** (2008) 1.
[19] D. Stamenkovic, I. Vasovic // *Scientific Technical. Rev.***12** (2009) 57.
[20] Z. Barsoum, *Residual stress analysis and fatigue assessment of welded steel structures* (Ph.D. Thesis, Kungliga Tekniska Hogskolan Stockholm, Sweden 2008).
[21] S.A. Tsirkas, P. Papanikos, T.H. Kermanidis // *Journal of Materials Processing Technology* **134** (2003) 59.
[22] *JMatPro 7.0 User's Guide* (Sente Software Ltd., Surrey, UK, 2013).
[23] ALUSELECT, European aluminum association, Brussels. Databank for aluminum alloys, properties, applications and standards, 1990.
[24] X.K. Zhu, Y.J. Chao // *Computers & Structures* **80** (2002) 967.
[25] *ABAQUS/standard user's manual, v. 6.10.* (Hibbitt, Karlsson and Sorensen, Inc., Pawtucket, RhodeIsland, USA, 2010).
[26] J.R. Davis, *Aluminum and aluminum alloys, ASM specially handbook* (ASM International, Materials Park, Ohio, USA, 1994).
[27] R.N. Peter Childs, *Practical temperature measurements* (Butterworth-Heinemann, Oxford, UK, 2001) 238-288.
[28] K. Ando, K. Nishiguchi, *Average temperature of the molten pool in TIG and MIG arc welding of steel and aluminum*, IIW Doc. 212-161-68, 1969.
[29] G.E. Dieter, In: *Mechanical metallurgy* (McGraw-Hill, USA 1976), p. 232-291.
[30] *ASM Metals Handbook, Heat treating* (ASM International, Materials Park, Ohio, USA, 1991) ch.8.
[31] H. Li, C. Zeng, M. Han, J. Liu, X. Lu // *Transactions of Nonferrous Metals Society of China* **23** (2013) 38.

[32] G.P. Dolan, J.R. Robinson // *Journal of Materials Processing Technology* 153-**154** (2004) 346.
[33] S. Claves, M. Watanabe // *Microscopy and Microanalysis* **12** (2006) 1410.
[34] C.E. Cross, D.L. Olson // *Welding Journal* **61** (1982) 381s-387s.
[35] G.F. Vander Voort, In: *Metallography and Microstructures* (ASM International, Materials Park, Ohio, USA, 1985), ch.10.
[36] P.M.G.P. Moriera, F.M.F de Oliveira, P.M.S.T. de Castro // *Journal of Materials Processing Technology* **207** (2008) 283.
[37] R.R. Ambriz, G. Barrera, R. García and V.H. López // *Welding International* **24** (2010) 42.
[38] J. Asensio-Lozano, B. Suárez-Peña, G.F. Vander Voort // *Materials* **7** (2014) 4224.